

Data-space cross-validation of global tomographic models to assess mantle structure underneath the Pacific Ocean

Mathurin D. Wamba¹, Frederik J. Simons¹, and Jessica C. E. Irving²

¹*Department of Geosciences, Princeton University, Princeton, NJ 08544, USA. E-mail: mw1685@princeton.edu*

²*School of Earth Sciences, University of Bristol, Bristol, UK*

1 December 2023

SUMMARY

Seismic tomography is a principal method for studying deep mantle plume structure. Imaging Earth's wavespeed anomalies is conditioned by seismic wave sampling, and the uneven distribution of receiving stations worldwide leaves several candidate plumes beneath various hotspots across the globe poorly resolved. We regionally evaluate two full-waveform global tomography wavespeed models, GLAD-M25 and SEMUCB-WM1, focusing on the mantle below the Pacific Ocean in the region of the South Pacific Superswell. This area contains multiple hotspots which may be anchored in the Large Low Shear-Velocity Province at the base of the mantle. The two models show similarities and differences in the target region. With a goal of guiding subsequent iterations in the GLAD model suite, we assess the quality of GLAD-M25 in the target region relative to its global performance using a regional partition of the seismic waveform data used in its construction. We evaluate synthetic waveforms calculated using the spectral-element method, based on how well they fit the data according to a variety of criteria measured across multiple seismic phases, wave types, and frequency bands. The distributions of travel-time anomalies that remain in GLAD-M25 are wider regionally than globally, suggesting comparatively insufficiently resolved seismic velocity structure in the region of interest. This will motivate regionally focused inversions based on a subset of the global data set, and the addition of data sampling new corridors, especially using ocean sensors. We compare GLAD-M25 and SEMUCB-WM1 by cross-validation with a new, independent, data set. Our results reveal that short- and long-wavelength structure is captured differently by the two models. Global models use misfit criteria that may strive for balance between portions of the data set, but could leave important regional domains underserved. Our results lead us to recommend focusing future model iteration and data addition on and around the Pacific Superswell to better constrain seismic velocity structure in this area of significant geodynamic complexity.

Key words: Tomography, Plumes, Global Seismology, Synthetic Seismograms

1 INTRODUCTION

Mantle upwellings play a vital role in Earth processes (Koppers et al. 2021), and when they take the form of narrow mantle plumes, they provide an essential window into the structure, composition, and dynamics of Earth's deep interior (Weis et al. 2023). Most volcanic hotspots are located in the oceans (Sleep 1990; Courtillot et al. 2003; King & Adam 2014), which cover two-thirds of Earth's surface. It is challenging to deploy seismic stations around ocean islands to increase imaging aperture (Wolfe et al. 2009; Maguire et al. 2018), which has led to biases in seismic imaging of mantle plumes compared to subduction zones (Montelli et al. 2006; Nolet et al. 2007). The latter have been rather well imaged by models (van der Hilst et al. 1993; Grand et al. 1997; Fukao et al. 2001) that have received sustained data addition and methodological improve-

ment (Li et al. 2008; Lu et al. 2019; Obayashi et al. 2013; Sigloch & Mihalynuk 2013). Observing seismic waves beneath the oceans requires specialized equipment and sensors such as ocean-bottom seismometers (Collins et al. 2001; Kohler et al. 2020), anchored (Slack et al. 1999; Sukhovich et al. 2014) or floating (Sukhovich et al. 2015; Simon et al. 2021) hydrophones at mid-column depths.

Several global tomographic models (Zhao 2004; Kustowski et al. 2008; Ritsema et al. 2011; French & Romanowicz 2015; Bozdağ et al. 2016; Lei et al. 2020) developed using different methodologies have provided evidence of broad low shear-wave speed zones beneath several major hotspots, providing insight into the structure of Earth's mantle plumes. The rise of buoyant plumes may be influenced by flow, circulation, and basal structure within the mantle (Steinberger 2000; Auermann et al. 2014; Nolet et al.

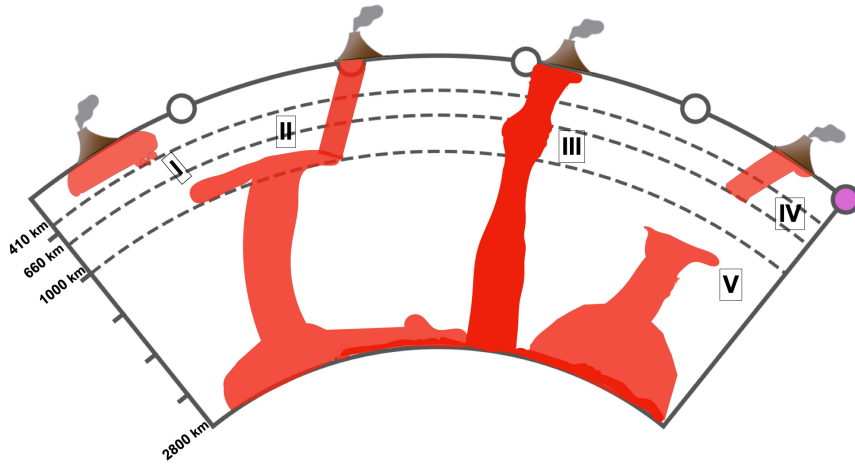


Figure 1. Sketch illustrating different types and morphologies of mantle plumes beneath hotspots as interpreted from mantle models. (I) Hotspots originating in the upper mantle. (II) Hotspots underlain by ponding zones in the mantle transition zone. (III) Mantle plume rising from the core-mantle boundary undeflected by mantle flow. (IV) Hotspots appearing to originate within the mantle transition zone, perhaps due to lack of model resolution. (V) Mantle plume rising from the core-mantle boundary may stall in the lower mantle without reaching the transition zone or the upper mantle.

2007), making their large-scale structure more complex than in the canonical Morgan (1971) hypothesis, which continues to generate lively debate (Foulger 2002). Seismic anisotropy is an important indicator of mantle flow (Fouch et al. 2001; Gaherty 2001; Benoit et al. 2013; Faccenda & VanderBeek 2023), though direct inference is significantly complicated by the mechanisms of microstructural fabric formation, and, in particular, the presence of water and partial melt (Karato et al. 2008). We will only consider isotropic elastic wave speed variations here. Intricate plume structures comprising ponding zones (Nolet et al. 2006; Wamba et al. 2021, 2023) and branching networks have been imaged, e.g., in the Indian Ocean beneath La Réunion (Tsekhmistrenko et al. 2021; Wamba et al. 2023) and in the Antarctic Rift System beneath Marie Byrd Land (e.g., Hansen et al. 2014). Beneath the Central Pacific around Hawaii, seismically slow material may have accumulated in the mid-mantle (Shen et al. 2003; Yu et al. 2018; Zhang et al. 2023).

Fig. 1 sketches a conceptual framework of plume structure types, and Fig. 2 shows a variety of cross-sections through the two global seismic tomography models that we will be assessing in this paper. Among the questions that we identify, which require the best achievable tomographic resolution to address, are: (I) Do some plumes originate within the upper mantle or from shallow sources of ponding material, either physically confined or tomographically poorly resolved (Anderson 2001; Foulger 2002)? (II) Might material sourced from the core-mantle boundary (CMB) region at 2800 km depth be ponding horizontally in or beneath the mantle transition zone between 660 and 1000 km, as it appears in some models (Nolet et al. 2006; Wamba et al. 2021, 2023), and as is perhaps also the case beneath Samoa? (III) Are there indeed mantle plumes rising vertically from the CMB to the upper mantle as suggested beneath Pitcairn by SEMUCB-WM1 (French & Romanowicz 2015; Marignier et al. 2020), unimpeded by mantle circulation and flow (Steinberger et al. 2004)? (IV) Can mantle plumes that rise from broad upwelling regions anchored at the CMB, as is apparently the case beneath Marquesas (Lei et al. 2020; French & Romanowicz 2015), stall in the lower mantle? (V) Do some hot-

spots originate from within or just below the mantle transition zone (Benoit et al. 2013; Burky et al. 2021), as suggested by the structure beneath Tahiti and Louisville, or does that reflect a lack of resolution? Does the Large Low Shear-Velocity Province at the CMB beneath Samoa and Tahiti give rise to multiple plume conduits (Garnero et al. 2016), as beneath La Réunion (Wamba et al. 2023)?

Seismic tomography model GLAD-M25 (Lei et al. 2020) was based on adjoint full-waveform inversion (Liu & Tromp 2008) of global seismic data from 1,480 earthquakes recorded at 11,800 seismic stations modeled using a spectral-element approach on a polynomial node grid (Komatitsch et al. 2000). This model improved upon first-generation model GLAD-M15 (Bozdağ et al. 2016), itself an update of S362ANI by Kustowski et al. (2008). Despite the large amount of data that was assimilated and the overall high model quality (see Fig. 2, left column), several hotspots in the Pacific (e.g., Louisville, Caroline, East Australia, Marquesas, Easter, Tahiti, Galápagos), remain poorly understood. Other hotspots in the region (e.g., Samoa, Macdonald, and Pitcairn), show evidence of whole-mantle plumes rising from the CMB to the upper mantle. Radial anisotropy in model GLAD-M25 is confined to the upper mantle. Insufficiently resolved structure may be ascribed to a combination of source uncertainty and an incomplete model parametrization, including the lack of azimuthal anisotropy (Becker et al. 2003), inherited topography on internal discontinuities (Burky et al. 2023), and heterogeneous attenuation (Lei et al. 2020).

Seismic tomography model SEMUCB-WM1 (French & Romanowicz 2014, 2015) used an inversion approach described by Lekić & Romanowicz (2011) that calculates sensitivity kernels using mode-coupling theory (Li & Romanowicz 1995) to build a whole mantle model parameterized in spherical splines (Wang & Dahlen 1995). Building on the starting models of Mégnin & Romanowicz (2000) and French et al. (2013), this model appears to reveal relatively similar mantle features beneath a number of identifiable hotspots (see Fig. 2, right column). SEMUCB-WM1 has a built-in one-dimensional attenuation model (Durek & Ekström 1996) and, like GLAD-M25, only considers radial anisotropy.

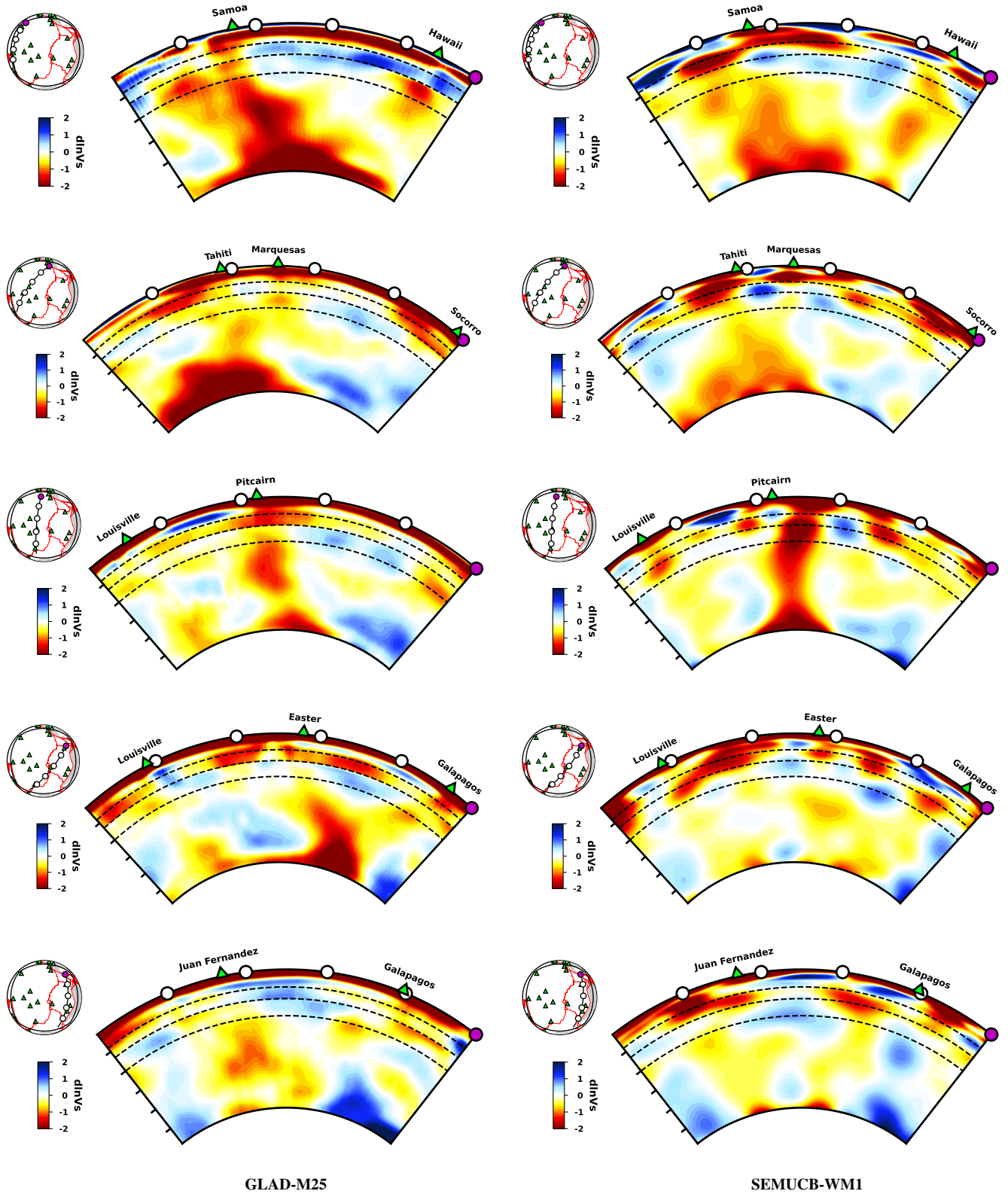


Figure 2. Shear-wave speed anomalies in the mantle according to global seismic tomography models GLAD-M25 (left column) and SEMUCB-WM1 (right). Cross-sections follow great-circle paths shown in the map inserts. Green triangles indicate hotspot locations (Steinberger 2000). Dashed black lines mark 410, 660, and 1000 km depth. Both models agree on the presence of mantle plumes below Samoa (top row) and Pitcairn (middle) as rising from the core-mantle boundary. Below Tahiti and Marquesas (second row) the models are in relative morphological agreement, though they are mismatched in amplitude. Beneath Easter and Galápagos (fourth), GLAD-M25 shows a low-velocity anomaly anchored at the core-mantle boundary, but no comparable structure is present in SEMUCB-WM1. GLAD-M25 has mantle structure that is inconsistent with SEMUCB-WM1 beneath Louisville (middle and fourth rows). GLAD-M25 maps more lower-mantle structure underneath Juan Fernandez hotspot than SEMUCB-WM1 (bottom).

Some hotspots (e.g., Tahiti, Easter) in Polynesia exhibit low-velocity anomalies in the lower and upper mantle, but not in the transition zone. Others (e.g., Marquesas, Louisville, Galápagos) show low-velocity structure primarily in the upper mantle. Do plumes have multiple possible origins in Earth’s mantle, or are the apparent differences due to lack of resolution owing to poor coverage and modeling approximations? Overall GLAD-M25 and SEMUCB-WM1 are compatible models, but the absence of plume structure beneath some known hotspots (e.g., Juan Fernandez, Louisville, Socorro, Easter Island) raises questions about the accuracy of either. In particular, it is unclear whether the fit between observed and simulated data influenced by structure within the Polynesian domain is as good as that reached by global evaluation.

To determine whether plume-like structures beneath Polynesian hotspots are well constrained, resolved, and accurately imaged, and to evaluate the potential for future inversions with or without additional data, we conduct two data-space assessments by computing and analyzing metrics relating observations to synthetic data simulated in both models. With regards to GLAD-M25, our first assessment focuses on a regional-versus-global evaluation of misfit via detailed comparisons of the travel-time anomaly distribution for a variety of wave types that are sensitive to the target region. As the region of interest we use a portion, or “chunk” of the cubed sphere (Ronchi et al. 1996), delineated by black lines in Fig. 3. For its comparison with SEMUCB-WM1, we assemble an independent, smaller, data set to calculate the similarities between synthetics and observations and perform a statistical analysis to ascertain whether apparent differences in model structure are warranted by the data.

This work is structured as follows. We first present the region under investigation and identify, from the database underlying the GLAD-M25 model, seismic event-station pairs that fall within the target region. We discuss the metrics relating the observed to the predicted data. We calculate histograms of relative travel-time anomalies within GLAD-M25 data in different categories and period bands, contrasting the regional subset with the global values. We perform comparisons between GLAD-M25 and SEMUCB-WM1 along similar lines, on the basis of an independent data set not involved in the construction of either model.

2 DATA AND METHODS

The published successor to GLAD-M15 (Bozdağ et al. 2016), GLAD-M25 was constructed using 1,480 earthquakes within the magnitude range $5.5 \leq M_w \leq 7.2$. To assess model quality at the regional scale we selected from the data used to build GLAD-M25 a subset that illuminates the target region. All 453 seismic sources and stations that fall inside the chunk are shown in Fig. 3. On the left, the sources are represented with focal mechanisms in different colors depending on their depth: yellow-white for deep earthquakes (>300 km) and red-white for shallow and intermediate earthquakes <300 km. In the middle, the stations comprise 117 ocean-bottom seismometers (green triangles) and 380 land seismometers (yellow inverted triangles). GLAD-M25 and SEMUCB-WM1 were cross-validated by selecting 11 recent events (from 2022) that were not included in the construction of either model, shown on the right. These were selected based on their isolated timing (i.e., without aftershocks and no simultaneous events), reasonable waveform qual-

ity (after manual inspection), and their reasonable moment magnitude ($M_w < 7.5$). Synthetic data in both models were calculated using SPEC3D-GLOBE (Komatitsch et al. 2000) and compared with the observed data corresponding to the same seismic ray path.

The travel-time anomaly ΔT is the time lag that maximizes the cross-correlation $C(\tau)$ between the observed, $d(t)$, and the synthetic, $s(t)$, seismograms in a window of length T starting at t_0 ,

$$\Delta T = \arg \max_{\tau} \{C(\tau)\}, \quad (1)$$

$$C(\tau) = \frac{\int_{t_0}^{t_0+T} [d(t) - \bar{d}] [s(t - \tau) - \bar{s}] dt}{\sqrt{\int_{t_0}^{t_0+T} [d(t) - \bar{d}]^2 dt \int_{t_0}^{t_0+T} [s(t - \tau) - \bar{s}]^2 dt}}, \quad (2)$$

with \bar{d} and \bar{s} the means of the data and the synthetic over the corresponding time interval. With this normalization, $C(\Delta T)$ is the cross-correlation coefficient between the overlapping segments of the observed and synthetic time series after shifting by ΔT . Without shifting, $C(0)$ is a measure of the data fit in the tomographic model at the current iteration.

If we forgo the indices t_0 and T , and label the discretized shifted time series d_i and s_i^τ , a concise notation is

$$C(\tau) = \frac{\sum_i (d_i - \bar{d})(s_i^\tau - \bar{s})}{\sqrt{\sum_i (d_i - \bar{d})^2 \sum_i (s_i^\tau - \bar{s})^2}}. \quad (3)$$

An alternative approach to measuring the fit between the predicted and observed seismograms is to compute the relative root-mean squared (rms) waveform difference,

$$R(\tau) = \frac{\sqrt{\sum_i (d_i - s_i^\tau)^2}}{\sqrt{\sum_i (d_i - \bar{d})^2}}. \quad (4)$$

A third metric is the amplitude anomaly between prediction and observation (Dahlen & Baig 2002; Maggi et al. 2009),

$$\text{dln}A(\tau) = \frac{1}{2} \ln \left[\frac{\sum_i (d_i - \bar{d})^2}{\sum_i (s_i^\tau - \bar{s})^2} \right]. \quad (5)$$

The resulting best-fit scaling factor is given by

$$\alpha = \exp[\text{dln}A(\Delta T)]. \quad (6)$$

For each window, metrics are computed at the time-shift that optimizes the cross-correlation, $\tau = \Delta T$, and at the current state of the model, $\tau = 0$. A negative travel-time anomaly, $\Delta T < 0$, signifies a late predicted arrival, i.e., a wavespeed model that is too slow over the average trajectory. A positive travel-time anomaly, $\Delta T > 0$, indicates an early predicted arrival, i.e., a model that is relatively too fast. Large relative travel-time shifts ΔT , and positive cross-correlation values $C(\Delta T)$ that are high relative to $C(0)$, indicate that the current model retains the potential for improvement. In that case, in principle, subsequent, regionally focused, model iterations (e.g., Zhu et al. 2012; Cui et al. 2023) should help improve the synthetics to approximate the observations more closely.

Examples of data, measurements, and metrics across a range of long and short paths, land-based and ocean-bottom seismic stations, are shown in Figs 4 and 5. Fig. 4 focuses on seismic body waves, and Fig. 5 highlights surface waves. All three-component waveforms were filtered into three period bands, 17–40 s, 40–100 s, and 90–250 s. The body waves were partitioned into the period ranges 17–40 s and 40–100 s, whereas the surface waves were split

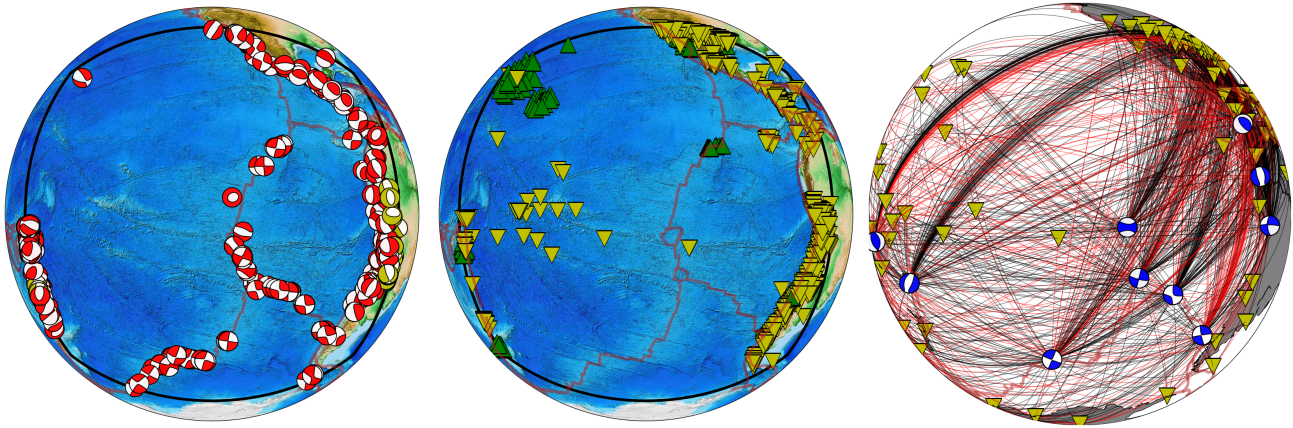


Figure 3. (Left) Focal mechanisms of 453 sources from the GLAD-M25 data set that fall within our region of interest (black bounding curve). White-yellow sources are over 300 km deep, white-red mechanisms are at shallower depths. (Middle) 380 land stations (yellow, inverted triangles) and 117 ocean-bottom seismometers (green triangles). (Right) Stations, earthquake locations and mechanisms and their ray paths from the independent data set used for cross-validation of two global seismic models, GLAD-M25 and SEMUCB-WM1. Travel-time anomalies of red paths exceed ± 5 s.

into the categories 40–100 s and 90–250 s. In addition to listing the cross-correlations $C(0)$ and $C(\Delta T)$, the amplitude measurements $d\ln A(0)$ and $d\ln A(\Delta T)$, both figures also quote the relative root-mean-squared (rms) waveform differences, $R(0)$ and $C(\Delta T)$.

GLAD-M25 relied on window selection by the package FLEXWIN (Maggi et al. 2009), which resulted in hundreds of thousands of seismogram segments. Some seismic traces have multiple windows that were measured, as is the case for the first waveform shown in Figs 4. The shaded areas list the current rms, $R(0)$, below the trace, and the current cross-correlation, $C(0)$, above it. Observed seismograms are in red, and the synthetics, computed in GLAD-M25, are in blue. For the zoomed-in portions, the aligned signal, phase and amplitude-corrected by advancing or delaying it by ΔT and scaled by α , is shown dashed in black. It is apparent that some waveforms are not completely optimized, yet can be made to fit well after future adjustments. That is the case for body and surface wave windows, for land stations and also for ocean-bottom-seismometer data.

3 RESULTS

As stated in Sec. 1, the first objective of this paper is to assess the potential for regional model improvement in our Pacific area of interest. This improvement may take the form of future full-waveform inversions of subsets of the data that cover the target region and/or by the addition of new data, especially corresponding to oceanic paths. To this end we perform an intra-comparison of adjoint model GLAD-M25 (Lei et al. 2020) by evaluating a piece of the model in the Pacific around French Polynesia against the whole globe, using the data that it was made of, and the synthetics from the last, i.e., the 25th, iteration.

Our second objective is to compare the GLAD-M25 model with SEMUCB-WM1 (French & Romanowicz 2015), an independent model that was made on the basis of sensitivity kernels computed using mode coupling theory. To further this goal we perform an inter-comparison in the same Pacific region enclosing French Polynesia using an independent validation set, with the selection of new windows carried out by FLEXWIN.

3.1 Distribution of travel-time anomalies

To understand the relative resolution of mantle structure beneath the Pacific Ocean, we examine a regionally targeted subset of the global data set that was used in building global model GLAD-M25. Figs 6 and 7 summarize the results of our analysis. We are presenting histograms of the travel-time-normalized travel-time anomalies, $\Delta T/T$, in percent. To compute these we simply divided the measured travel-time anomalies by the time of the midpoint of the measurement window, measured relative to the earthquake origin time. To first order, these metrics approximate the relative velocity anomaly, $\Delta c/c$, averaged over the path sampled by the specific phases, with c equal to the P -, S -, or surface-wave phase speed.

There are twelve different categories in all: two dominant wave types (body and surface), three components (radial, transverse, and vertical) and three period bands (one shared between the body and surface waves). The number of measurement windows represented by histograms in each category, N , is reported in the annotation of each panel. The number of bins, n , in each histogram follows Sturges' rule, $n = 1 + \log_2(N)$, where N is the number of data. For the tabulated values shown inside the panels of Figs 6 and 7 we report both trimmed (between the 3% and 97% percentiles) and untrimmed (0% to 100%) statistics, as listed at the top of each summary table. Gaussian probability density functions with the means and variances calculated after trimming are superimposed. Histograms for the global data set are shown right side up, whereas for the regional subsets, we flipped them upside down.

The body-wave relative travel-time distributions drawn in Fig. 6 show larger anomalies in the regional domain than at the global scale, with more windows displaying $|\Delta T/T| \geq 0.5\%$ regionally. Comparing the global and regional distributions for body waves between 17–40 s, Figs 6a–c show that the regional standard deviation is twice that of the global value. As frequency decreases and we consider long-period body waves between 40–100 s period, Figs 6d–f, the standard deviations increase, and the regional standard deviations remain larger than their global equivalents. Similar observations are to be made for surface waves, as revealed by the distributions given in Fig. 7, for the wave packets filtered between

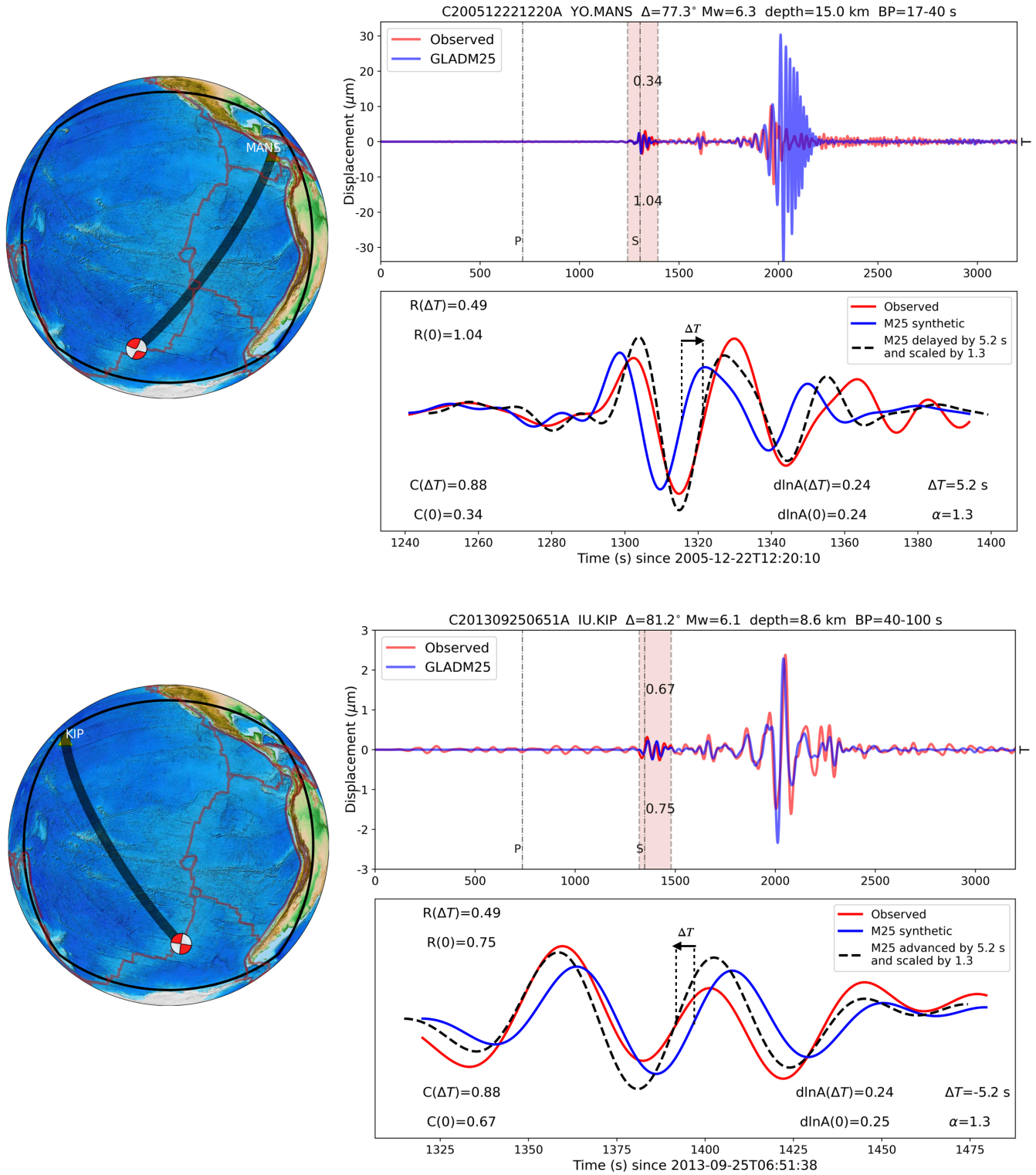


Figure 4. Ray paths, seismograms, and waveform metrics for body waves in two period bands, 17–40 s (*top set*), and 40–100 s (*bottom*). Each three-panel set presents a map view with the surface ray path connecting the earthquake source to the receiver (*left*), and the subfigures (*right*) show a whole seismogram (*top*) and a zoom on the windowed *S* wave (*bottom*). Observed seismograms are red, the predictions, computed in GLAD-M25, in blue. In the zoomed-in sections, the synthetic seismograms are also shown, as dashed black lines, after shifting by the signed amount of the travel-time anomaly measurement, ΔT , and scaled by the factor $\exp[d\ln A(\Delta T)]$, which brings them into maximal alignment, as measured by the value of the cross-correlation coefficient, $C(\Delta T)$. In the top cluster, the travel-time anomaly is positive, $\Delta T = 5.2$ s, indicating that the synthetic arrives earlier than the observed waveform (model GLAD-M25 is too fast). The scaled synthetic is delayed to align with the observations. In the bottom set, the anomaly is negative, $\Delta T = -5.2$ s, signifying a measurement in which the synthetic is late (hence the model too slow). The scaled synthetic is advanced into alignment, as shown.

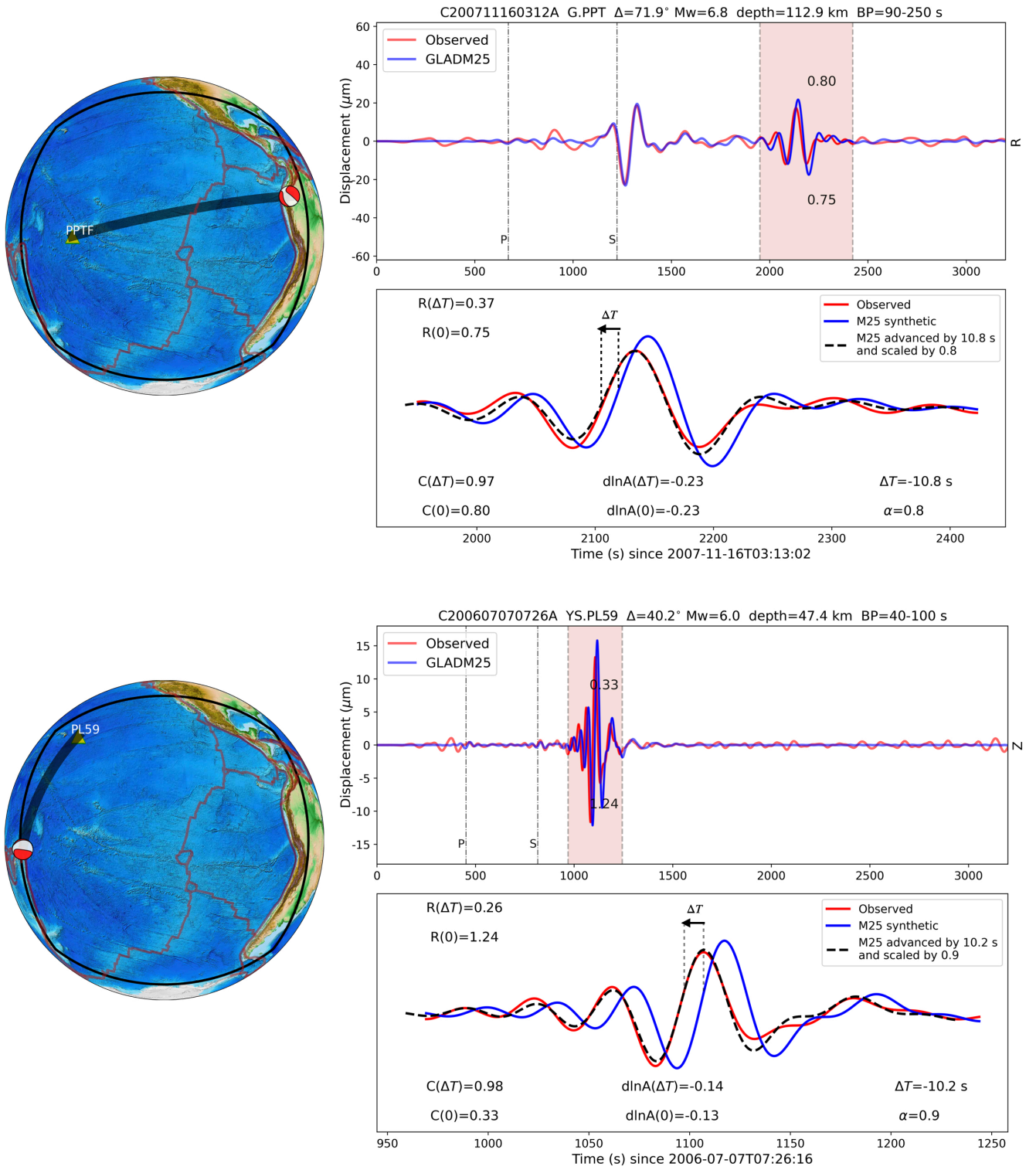


Figure 5. Ray paths, seismograms, and waveform metrics for surface waves in period bands, 90–250 s (*bottom set*) and 40–100 s (*top*). Labeling and layout are identical to Fig. 4, with observed seismograms in red, GLAD-M25 synthetics in blue, and the dashed black traces showing the phase-and-amplitude corrected synthetic that is maximally aligned with the observations. Note that Fig. 4 showed two transverse (T) component seismograms, whereas in this figure, we show one radial (R) component and one vertical (Z) component case, as indicated by the labels to the right of the top panels of every set. The top seismograms are for a long oceanic path that is recorded on island station PPT (in Papeete, Tahiti). The bottom seismograms are for a shorter oceanic path recorded by an ocean-bottom seismometer from the PLUME deployment (Laske et al. 2009). In both cases, the relevant wavespeeds in model GLAD-M25 are too slow for the trajectory. The synthetics need to be scaled and advanced by 10.8 s and 10.2 s, respectively, to bring them into maximal alignment with the observations, as measured by the cross-correlation metric.

periods 90–250 s, Fig. 7g–i, and between 40–100 s, Fig. 7j–l, which are sensitive down to the transition zone and to the upper mantle, respectively. Again the global remaining travel-time anomalies show a relatively Gaussian distribution centered at zero. On the other hand, the distributions of the regional travel-time anomalies are slightly shifted from the global distributions, and they appear flatter, with more outliers in the tails. Our interpretation of these results is that significant exploitable structure remains in the current data set, indicative of structure underneath the target region that is relatively more poorly resolved than the globe as a whole.

To evaluate the contribution of ocean-bottom seismometers (OBS) to the Pacific portion of global seismic model GLAD-M25, Fig. 8 presents a comparison of the travel-time anomaly distributions within the target region for land-based and OBS stations. Very few OBS measurements (less than 2% of the total) were included in the model, either in the body-wave or surface-wave categories. No OBS measurements were made on the horizontal components, which are generally noisier (Webb & Crawford 2010; Bell et al. 2015). The majority of the OBS measurements are in the 17–40 s body wave window, where the mean and standard deviation of the anomalies correspond well to the land-based observations. In the lower frequency bands there are fewer OBS data (less than 1000 in all cases, and only ~ 100 for the lowest frequency window). The smaller number of lower-frequency OBS data make it harder to draw conclusions about the possible differences in travel-time anomaly distributions. Given the limited contribution of OBS data to this model, incorporating more marine data, whether from stationary or mobile instrumentation (Nolet et al. 2019), may considerably improve the spatial distribution of the measurements and the tomographic model in this area.

3.2 Data-space model intercomparison

The data sets and methodology used to develop global models GLAD-M25 (Lei et al. 2020) and SEMUCB-WM1 (French & Romanowicz 2015) are distinct, and hence it is to be expected that the resolution of mantle structure differs between both models.

The cross-section comparisons shown in Fig. 2 made it clear that both models do reveal mantle plumes beneath certain hotspots such as Samoa and Pitcairn, with differences mostly affecting model amplitudes: for example, the low shear-velocity anomaly beneath Samoa is stronger in GLAD-M25 than in SEMUCB-WM1, whereas in SEMUCB-WM1 the anomaly amplitude beneath Pitcairn is stronger than in GLAD-M25. In certain regions the lower-mantle structures are rather different in both models, for example, a low shear-velocity structure that appears in GLAD-M25 beneath the Easter Island, Galápagos and Juan Fernandez hotspots is not present in SEMUCB-WM1. Both models show different upper-mantle features across Louisville, Easter, Galápagos, and Pitcairn hotspots. SEMUCB-WM1 exhibits a low-velocity structure beneath the Louisville hotspot that appears to rise from the mantle transition zone, which is nevertheless nonexistent in GLAD-M25. To what extent are any of these structures, and any of these structural differences, warranted by the data?

Rather than comparing models through difference images or vote maps, via correlations, spectral content, or other statistics, as has been the tradition in the literature (see Sec. 4), we examine how

the model differences might impact seismic waveforms themselves. To this end we produce an independent set of cross-validation data, and compute a second series of metrics as discussed in Sec. 2, suitable for exposing the differences between models through the data fits that they achieve. Fig. 3c showed the path coverage achieved for this part of the analysis. Note that the sensitivities of the seismic waves are much broader than rays (e.g., Hung et al. 2001).

Fig. 9 shows the details of how, for each event-station pair, we measured the cross-correlation between the observed and the predicted data, and the resulting travel-time anomaly, for synthetics newly computed in both models, on several time-windows. For this particular case, SEMUCB-WM1 exhibits favorable correlation values and travel-time anomalies for Rayleigh waves compared to GLAD-M25, while GLAD-M25 shows a better fit for Love waves. Although for surface waves both models predict arrivals which are later than the observed data, SEMUCB-WM1 is faster than GLAD-M25 for Rayleigh waves, whereas GLAD-M25 is faster than SEMUCB-WM1 for Love waves. For body waves, any preference between SEMUCB-WM1 and GLAD-M25 is dependent on the specific choice of comparison window. As remarked upon in Sec. 1, important caveats are that while both models are parameterized to capture radial anisotropy, azimuthal anisotropy is wholly missing from the analysis, and the treatment or lack thereof of attenuation is another factor that may preclude truly “fair” comparisons between both models, and between data sets that may contain the unmodeled effects of anisotropy and anelasticity that are likely present in the “true” Earth (Karato 1993, 1998).

In the vein of Figs 6–7, we computed travel-time anomaly distributions, Figs 10 and 11, for body and surface waves in the same period bands as before. For the body waves the residual anomalies in the band 17–40 s, Figs 10a–c, display histograms with heavy tails for both models. This behavior is much less pronounced in the 40–100 s band, Figs 10d–f. We interpret this as unresolved short-wavelength structure in both models. Note, SEMUCB-WM1 was based on body-wave data with a maximum period of 32 s (French & Romanowicz 2015). The difference between the models is furthermore expressed in the surface waves, whose distributions are less centered and relatively shifted, especially in the period band of 90–250 s on all three components, see Figs 11j–l.

4 DISCUSSION

The two global seismic tomography models, GLAD-M25 and SEMUCB-WM1 that we compared in the Pacific Ocean show prominent low-velocity anomalies in many similar locations throughout the mantle. Some of the differences are in amplitude, which might reflect variable levels of damping and other forms of regularization (Bozdağ & Trampert 2010), not to mention unavoidable biases due to choices of parameterization, especially with regards to anisotropy and attenuation. All tomographic models are inevitably filtered versions of the Earth (Ritsema et al. 2007), hence all direct data comparisons, especially in regions that comprise geodynamically anomalous or geologically unique provinces (Ekström & Dziewoński 1998), will be impacted by the specific modeling choices made (Koelemeijer et al. 2018).

More significant are the discrepancies in the lower mantle, e.g., beneath the Easter, Galápagos, and Juan Fernandez hotspots.

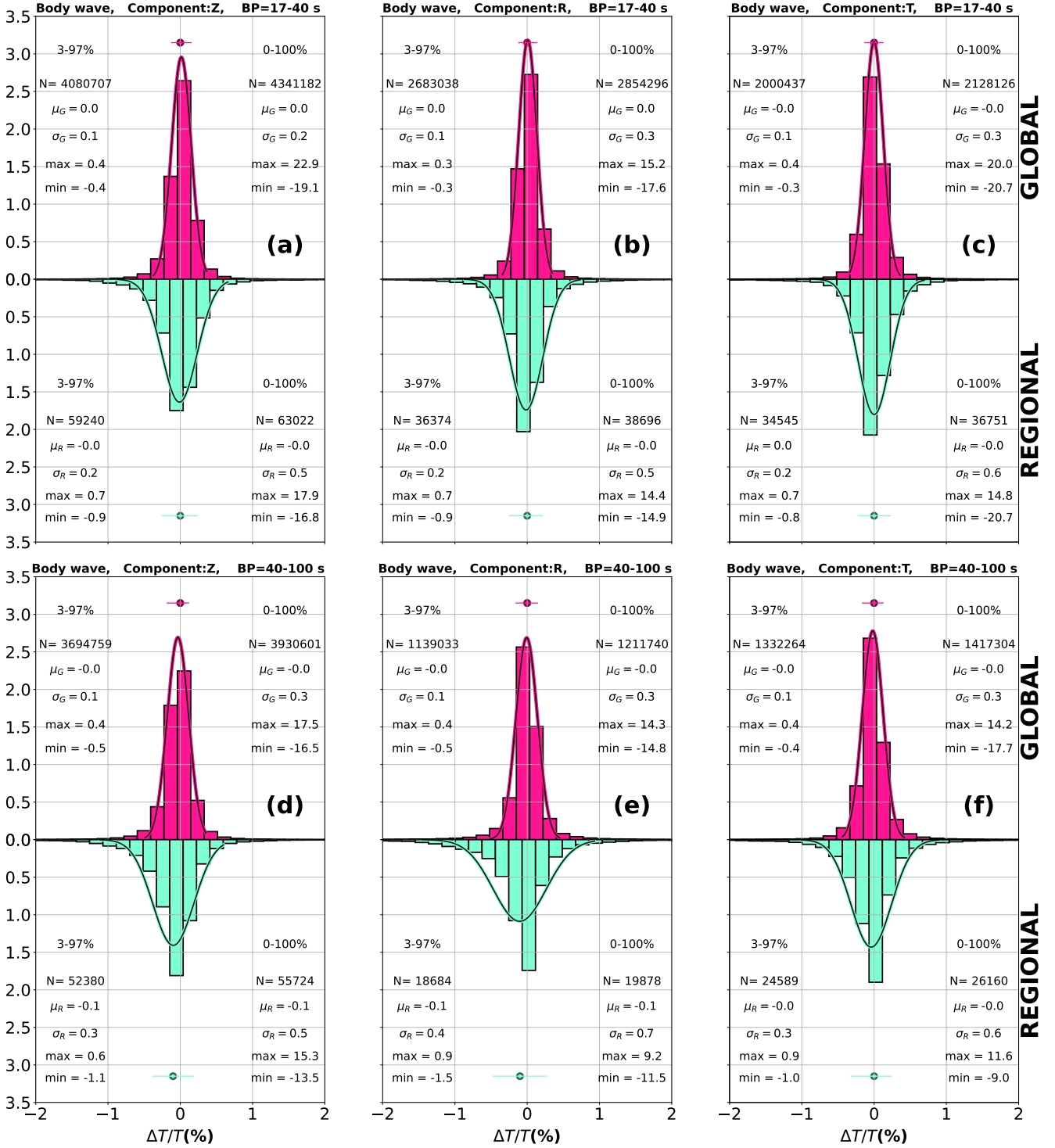


Figure 6. Distribution of normalized travel-time anomalies that persist in adjoint-based seismic tomography model GLAD-M25, for the Pacific target region and as compared to the entire globe. Histograms are shown for body waves across three seismogram components (vertical Z, radial R, and transverse T) and in two period bands, 17–40 s (*top row, a–c*) and 40–100 s (*bottom row, d–f*). Histograms of all global measurements are shaded red, those of the regional subsets are in green, shown upside down. Means and plusminus one standard deviation ranges hover over the bar graphs. Normal distributions are superimposed as solid curves. Values listed on the left side of every panel are computed after removing outliers not within the 3rd–97th percentile range, whereas the values on the right were computed using all of the data for each category. All global averages are indistinguishable from zero, and all global standard deviations are 0.1 s, suggesting unbiased model residuals and globally extremely tight data fits. Regional distributions are only slightly offset from zero, but their standard deviations are two to three times larger than the global values. The regional distributions also have heavier tails, suggesting that a sizable fraction of the data remains to be fully explained by the wavespeed model in the region.

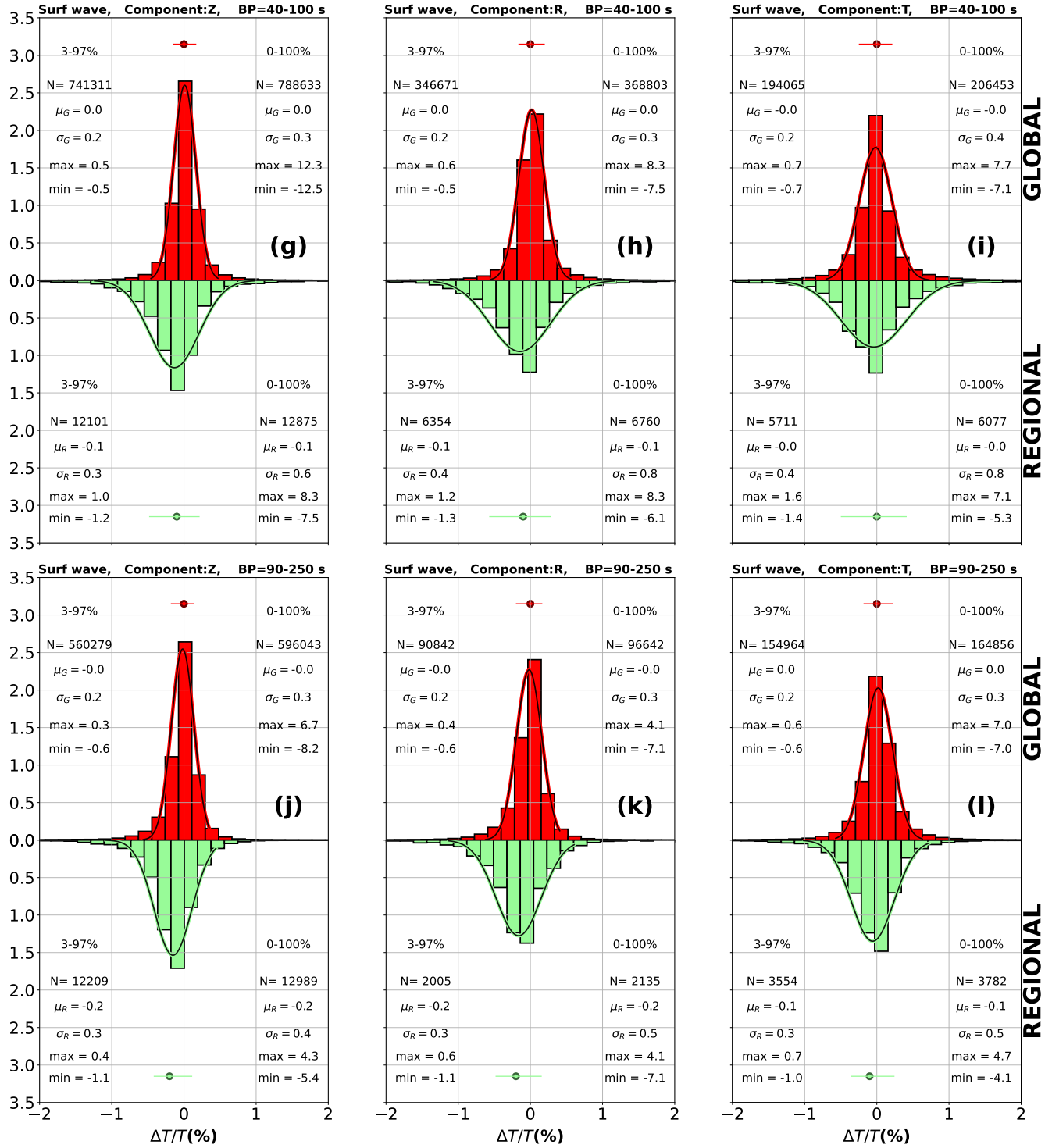


Figure 7. Distribution of normalized travel-time anomalies persisting in model GLAD-M25, for the Pacific target region as compared to the whole globe. Histograms are for surface waves across three seismogram components (vertical Z, radial R, transverse T) in period bands 40–100 s (*top row, g–i*) and 90–250 s (*bottom row, j–l*). Layout and labeling are exactly as in Fig. 6. Again, the global distribution is always centered on zero within each category. In contrast, the regional distributions are shifted slightly towards more negative values, showing increased standard deviations and stronger contributions from the tails.

Even though the structure beneath the Pitcairn hotspot appears better defined in SEMUCB-WM1 than in GLAD-M25, the plume conduit is located in the same region in both models. GLAD-M25 exhibits an apparent lack of resolution in the transition zone between 1000 and 600 km and in the lowermost mantle. Beneath Hawaii, the

SEMUCB-WM1 model tends to capture a weak low-velocity conduit, unlike GLAD-M25. A shear low-velocity structure observed beneath Samoa in both models is more pronounced in GLAD-M25 than in SEMUCB-WM1.

Seismological model and data comparisons may take many

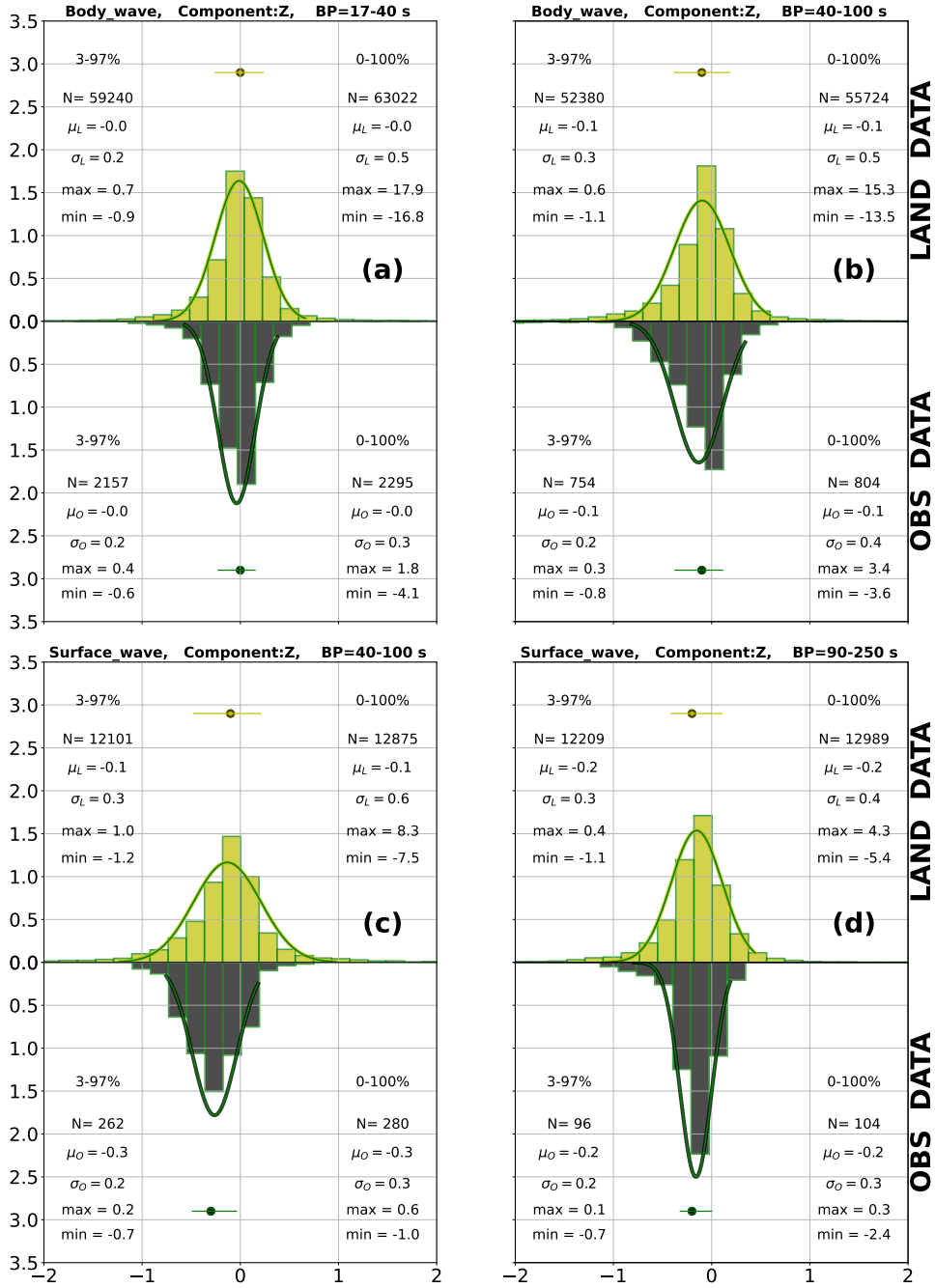


Figure 8. Distribution of normalized travel-time anomalies that persist in tomography model GLAD-M25, comparing measurements made inside the Pacific target region at land-based stations (yellow) versus ocean-bottom seismometers (black), for the vertical (Z) component recording body waves in the period bands 17–40 s and 40–100 s (a–b), and surface waves in the bands 90–250 s and 40–100 s (c–d). Note that comparatively very few OBS measurements were used in the construction of GLAD-M25, and none were made on the radial or transverse components. Layout and labeling are as in Figs 6–7.

forms (Moulik et al. 2022). Numerous authors have conducted detailed inter-model evaluations, on the basis of a variety of measures which are relatively straightforward to obtain from images, plan-forms, and cross-sections. These include correlation-based comparisons and confrontations with geodynamic models (e.g. Jordan et al. 1993; Rudolph et al. 2015), vote-mapping based consistency checks (e.g. Shephard et al. 2017) consensus-based cluster analyses (e.g., Lekić et al. 2012; Cottaar & Lekić 2016) spectral cross-model comparisons and grand averaging to an agreed-upon “best” model

(e.g., Becker & Boschi 2002), and statistical measures characterizing the relative distributions of anomalies (e.g., Hernlund & Houser 2008). Direct data comparisons (Ritsema et al. 2002; Bozdağ & Trampert 2010), in contrast, have been relatively rare. While the computational cost of data-space cross-validations is higher, they lead to a more focused identification of the geographical areas that are most in need of, or present most promise for, improvement.

Metrics relating observations to data predicted via spectral-element modeling in both models made on an independent data

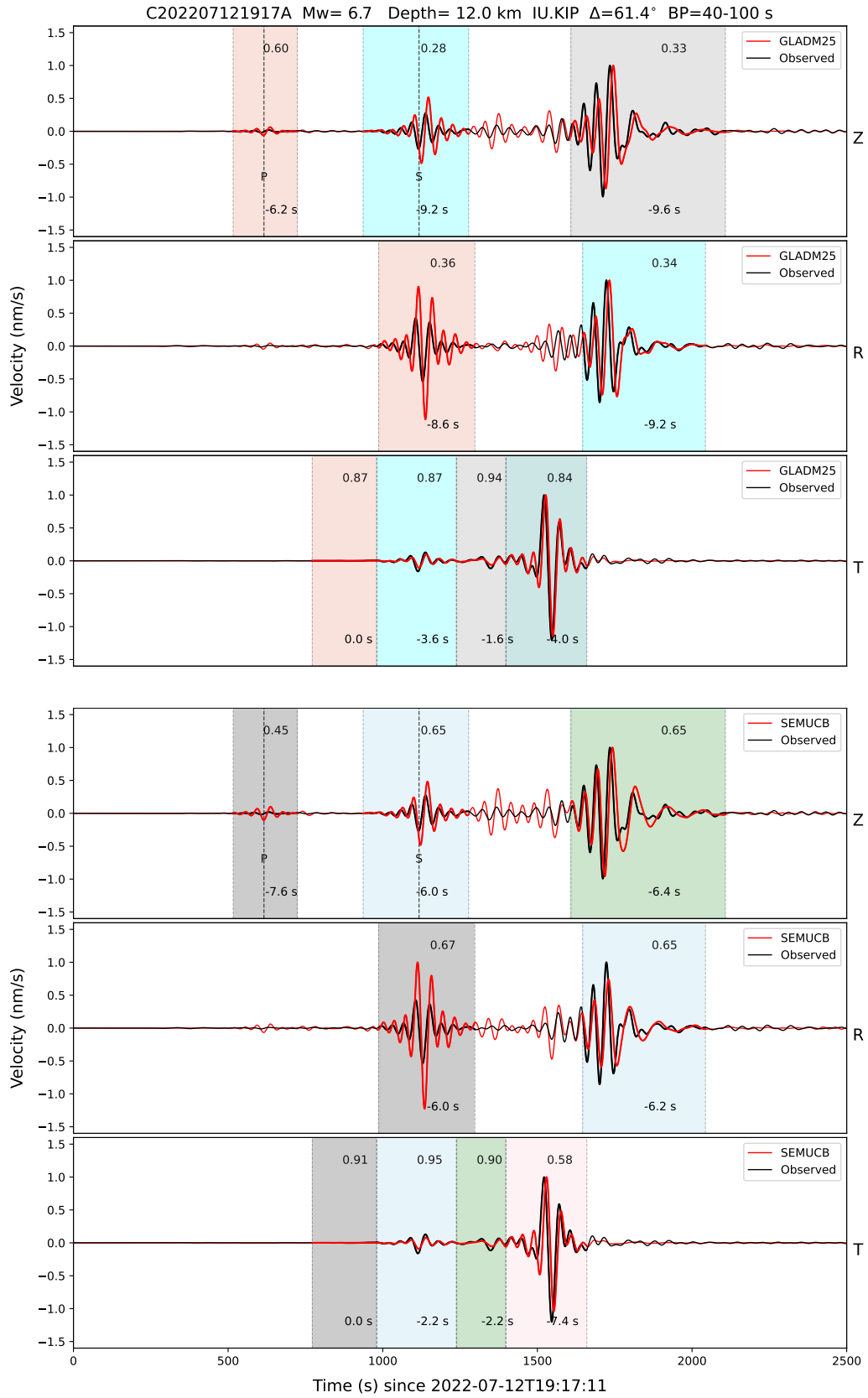


Figure 9. Comparison of the waveforms predicted in GLAD-M25 (top) and SEMUCB-WM1 (bottom) with the observed data (black) derived from event C202207121917A recorded at the central-Pacific seismic station KIP (Kipapa, Hawaii, USA). Comparison is performed in the same window, in the period range of 40–100 s, which includes body and surface waves. The correlation between the observed and predicted data is shown at the top of each window, and the travel-time anomaly is at the bottom. The event used for our comparison was not used in building either model.

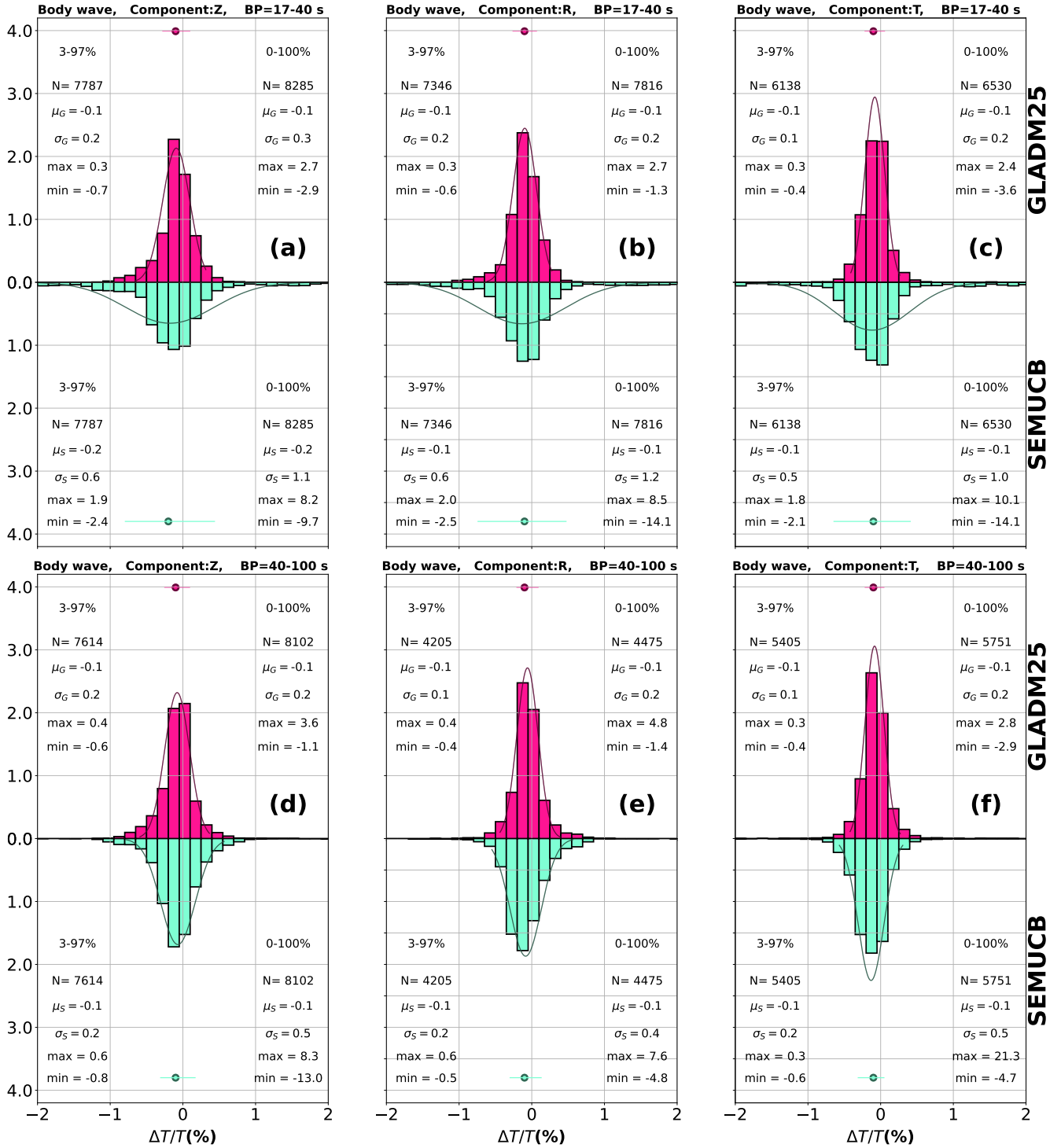


Figure 10. Normalized travel-time anomalies, measured on an independent data set covering the Pacific target region, that persist in GLAD-M25 (red histograms) and SEMUCB-WM1 (green, upside-down). Body waves are separated into two period bands, 17–40 s (a–c) and 40–100 s (d–f). In the period range 17–40 s the travel-time anomaly distribution in SEMUCB-WM1 is less Gaussian, and the standard deviations are markedly larger than in GLAD-M25.

set indicate a mixture of relatively good and relatively poor fits throughout the various time and phase windows analyzed, as shown in the example of Fig. 9. On the whole, travel-time anomalies and correlation coefficients between synthetic and observed data windows do still exhibit relatively low and high values, respectively, for both models. The similarity between both models is greatest in

the period band of 40–100 s for both body and surface waves. The discrepancy observed on long-period surface waves, in the period range 90–250 s may motivate the construction of a regional upper-mantle model in the South Pacific.

However, travel-time anomalies in the independent data set are larger than in the data used for the construction of GLAD-M25. The

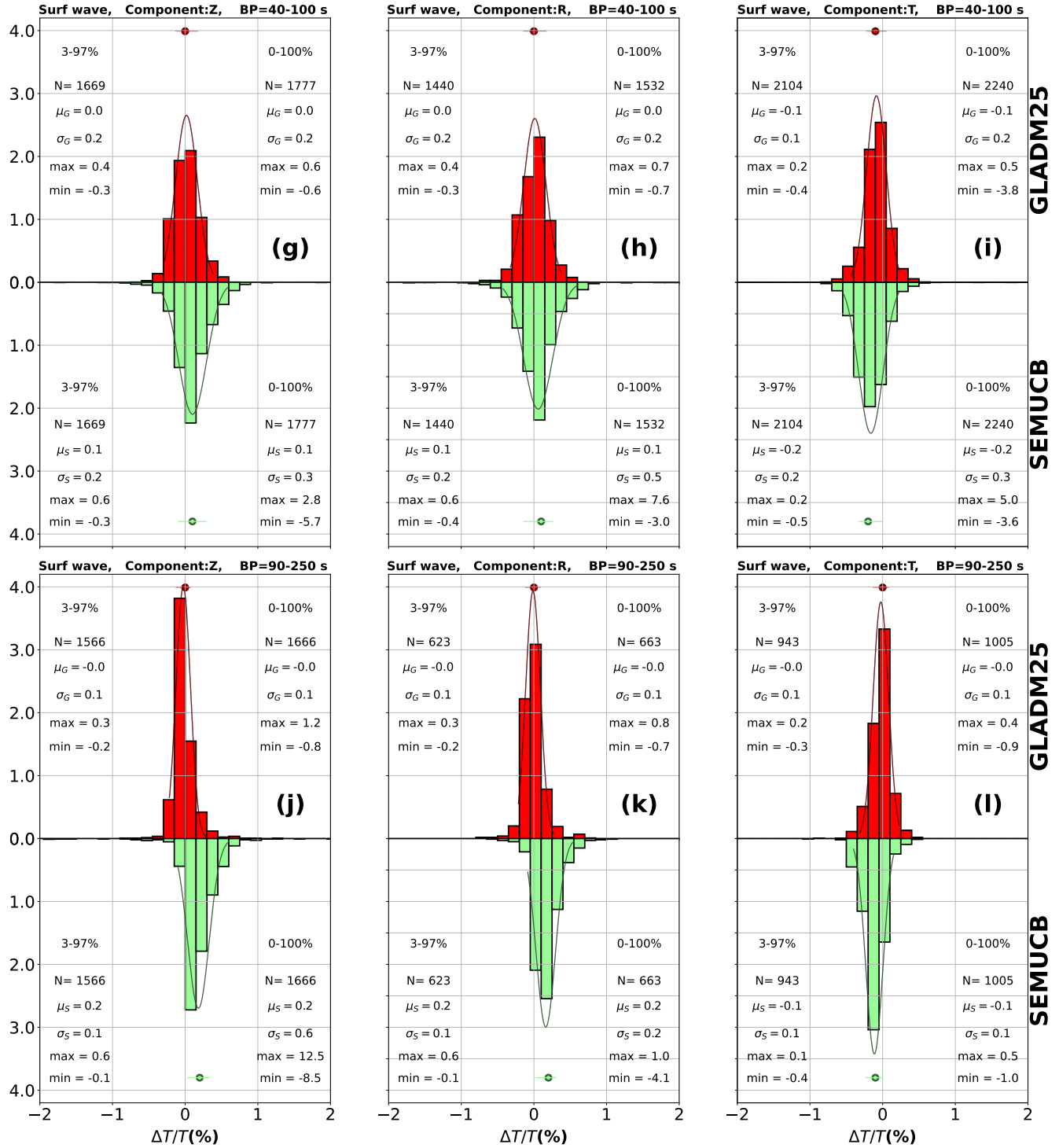


Figure 11. Distribution of normalized travel-time anomalies, made on an independent data set covering the Pacific target region, comparing GLAD-M25 to SEMUCB-WM1, laid out as for the body waves shown in Fig. 10, but now for surface waves, divided in two-period bands, 90–250 s (g–i) and 40–100 s (j–l).

comparison of our regional data-space results with assessment tests performed on “held-back” data sets used during the construction of both global models GLAD-M25 and SEMUCB-WM1 (Lei et al. 2020; French & Romanowicz 2014), suggests the held-back sets are better fit in terms of their average travel-time anomalies, with lower residual standard deviations. However, this reinforces our interpretation that global models require probing and evaluation in

specific geographic regions, as this allows us to focus on seismic ray paths that cross the target region, thereby sampling the relevant geological structures of most interest. It is precisely in those areas of great geodynamical importance, i.e., in the plume-rich region underlying the Pacific Superswell (McNutt & Fischer 1987; McNutt & Judge 1990; McNutt 1998), that new observations are hard to come by with traditional instrumentation (Simon et al. 2022).

5 CONCLUSIONS

Despite carefully designed weighting schemes to balance the relative geographic contributions of different data sets to tomographic inversions for global models (e.g., Ruan et al. 2019; Cui et al. 2023), regional portions of the globe may remain relatively under-resolved compared to the global average (a problem not confined to seismology, nor to this planet Plattner & Simons 2015). Global models GLAD-M25 (Lei et al. 2020) and SEMUCB-WM1 (French & Romanowicz 2015), obtained independently, have been very well received in the geophysical literature, and they have proved useful in the interpretation of other signals of deep Earth processes, such as those provided by geochemical analyses (Williams et al. 2019).

In this paper we first performed a regional assessment of the quality of GLAD-M25 in a Pacific target region centered on Polynesia, in order to ascertain its resolution of mantle structure and the potential for improvement by conducting subsequent regionally-focused model iterations and the addition of new data, especially those sampling oceanic paths measured at ocean-bottom stations or floating sensors available from past or future deployments. We studied the distribution of travel-time anomalies over a regionally selective subset of the data, obtained by the spectral-element method, as compared to the global data set that was used in constructing the model. The relatively significant discrepancy that still exists between the observed and predicted waveforms supports our finding that it is likely that unresolved plume structure exists beneath several hotspots in the Pacific Ocean around French Polynesia. The travel-time anomaly distribution retains larger values in the target region than over the entire globe. Numerous waveforms recorded by seismic stations around Polynesia still show significant shifts when compared with the synthetic predictions. Our data analysis furthermore highlights the rather minor contribution of ocean-bottom-seismometer data to the current model, and the significant potential for data addition from existing deployments, especially from the horizontal components.

In addition to the regional intra-comparison of GLAD-M25, we performed a model inter-comparison between GLAD-M25 and SEMUCB-WM1. Simply comparing models based on selected cross-sections and depth slices, i.e., in model space, as has been the norm in comparative tomography, cannot reveal the impact of differences on seismic waveforms. Here we cross-validated both models in data space, by analyzing the distribution of waveform fits newly calculated for an independent data set. Models GLAD-M25 and SEMUCB-WM1 show discrepancies at shorter periods, between 17–40 s, where the travel-time anomaly distribution in SEMUCB-WM1 shows biases that remain undigested. At longer periods, between 90–250 s, discrepancies between surface-wave data fits differ for Love and Rayleigh waves. While both models are generally compatible with each other, and compatible with their own data sets, our independent analysis will motivate and inform the design of future studies conducting regional tomography targeting the Pacific region in efforts to image currently unresolved seismic velocity anomaly structure, especially underneath hotspots.

DATA AVAILABILITY

The complete data sets are available from the authors. Small, curated examples of our data sets and measurements are available on <https://github.com/wambis/Polynesia>.

ACKNOWLEDGMENTS

This research work was partially funded by a Princeton Presidential Fellowship to the lead author, which is gratefully acknowledged, and by NSF OCE-1917058 to FJS and JCEI. The authors thank Jeroen Tromp and Wenjie Lei for providing the global data set that enabled us to evaluate GLAD-M25, and Barbara Romanowicz for providing the subroutines that enabled the computation of synthetic seismograms in SEMUCB-WM1, and for valuable discussions.

REFERENCES

- Anderson, D. L., 2001. Top-down tectonics?, *Science*, **293**, 2016–2018.
- Austermann, J., Kaye, B. T. & Mitrovica, J. X., 2014. A statistical analysis of the correlation between large igneous provinces and lower mantle seismic structure, *Geophys. J. Int.*, **197**(1), 1–9, doi: 10.1093/gji/ggt500.
- Becker, T. W. & Boschi, L., 2002. A comparison of tomographic and geodynamic mantle models, *Geochem. Geophys. Geosys.*, **3**(1), 1003, doi: 10.1029/2001GC000168.
- Becker, T. W., Kellogg, J. B., Ekström, G. & O’Connell, R. J., 2003. Comparison of azimuthal seismic anisotropy from surface waves and finite-strain from global mantle-circulation models, *Geophys. J. Int.*, **155**(2), 696–714, doi: 10.1046/j.1365-246X.2003.02085.x.
- Bell, S. W., Forsyth, D. W. & Ruan, Y., 2015. Removing noise from the vertical component records of ocean-bottom seismometers: Results from year one of the Cascadia Initiative, *B. Seismol. Soc. Am.*, **105**(1), 300–313, doi: 10.1785/0120140054.
- Benoit, M. H., Long, M. D. & King, S. D., 2013. Anomalously thin transition zone and apparently isotropic upper mantle beneath Bermuda: Evidence for upwelling, *Geochem. Geophys. Geosys.*, **14**(10), 4282–4291, doi: 10.1002/ggge.20277.
- Bozdağ, E. & Trampert, J., 2010. Assessment of tomographic mantle models using spectral element seismograms, *Geophys. J. Int.*, **180**(3), 1187–1199, doi: 10.1111/j.1365-246X.2009.04468.x.
- Bozdağ, E., Peter, D., Lefebvre, M., Komatitsch, D., Tromp, J., Hill, J., Podhorszki, N. & Pugmire, D., 2016. Global adjoint tomography: first-generation model, *Geophys. J. Int.*, **207**(3), 1739–1766, doi: 10.1093/gji/ggw356.
- Burky, A., Irving, J. C. E. & Simons, F. J., 2021. Mantle transition zone receiver functions for Bermuda: Automation, quality control, and interpretation, *J. Geophys. Res.*, **126**(3), e2020JB020177, doi: 10.1029/2020JB020177.
- Burky, A., Irving, J. C. E. & Simons, F. J., 2023. The mantle transition zone beneath eastern North America: Receiver functions and tomographic velocity models, *Phys. Earth Planet. Inter.*, **340**, 107035, doi: 10.1016/j.pepi.2023.107035.
- Collins, J. A., Vernon, F. L., Orcutt, J. A., Stephen, R. A., Peal, K. R., Wooding, F. B., Spiess, F. N. & Hildebrand, J. A., 2001. Broad-band seismology in the oceans: Lessons from the Ocean Seismic Network Pilot Experiment, *Geophys. Res. Lett.*, **28**(1), 49–52, doi: 10.1029/2000GL011638.
- Cottaar, S. & Lekić, V., 2016. Morphology of seismically slow lower-mantle structures, *Geophys. J. Int.*, **207**(2), 1122–1136, doi: 10.1093/gji/ggw324.
- Courtillot, V., Davaille, A., Besse, J. & Stock, J., 2003. Three distinct types of hotspots in the Earth’s mantle, *Earth Planet. Sci. Lett.*, **205**(3–4), 295–308, doi: 10.1016/S0012-821X(02)01048-8.
- Cui, C., Bachmann, E., Peter, D. B., Liu, Z. & Tromp, J., 2023. Source-encoded waveform inversion in the Northern Hemisphere, *Geophys. J. Int.*, **235**, 2305–2322, doi: 10.1093/gji/ggad363.
- Dahlen, F. A. & Baig, A., 2002. Fréchet kernels for body-wave

- amplitudes, *Geophys. J. Int.*, **150**, 440–466, doi: 10.1046/j.1365-246X.2002.01718.x.
- Durek, J. J. & Ekström, G., 1996. A radial model of anelasticity consistent with long-period surface-wave attenuation, *B. Seismol. Soc. Am.*, **86**(1A), 144–158, doi: 10.1785/BSSA08601A0144.
- Ekström, G. & Dziewoński, A. M., 1998. The unique anisotropy of the Pacific upper mantle, *Nature*, **394**(6689), 168–172.
- Faccenda, M. & VanderBeek, B. P., 2023. On constraining 3D seismic anisotropy in subduction, mid-ocean-ridge, and plume environments with teleseismic body wave data, *J. Geodyn.*, **158**, 102003, doi: 10.1016/j.jog.2023.102003.
- Fouch, M. J., Fischer, K. M. & Wyssession, M. E., 2001. Lowermost mantle anisotropy beneath the Pacific: Imaging the source of the Hawaiian plume, *Earth Planet. Sci. Lett.*, **190**(3–4), 167–180, doi: 10.1016/S0012-821X(01)00380-6.
- Foulger, G. R., 2002. Plumes, or plate tectonic processes?, *Astron. Geoph.*, **43**(6), 6–19, doi: 10.1046/j.1468-4004.2002.43619.x.
- French, S., Lekic, V. & Romanowicz, B., 2013. Waveform tomography reveals channeled flow at the base of the oceanic asthenosphere, *Science*, **342**(6155), 227–230, doi: 10.1126/science.124151.
- French, S. W. & Romanowicz, B., 2015. Broad plumes rooted at the base of the Earth's mantle beneath major hotspots, *Nature*, **525**, 95–99, doi: 10.1038/nature14876.
- French, S. W. & Romanowicz, B. A., 2014. Whole-mantle radially anisotropic shear velocity structure from spectral-element waveform tomography, *Geophys. J. Int.*, **199**(3), 1303–1327, doi: 10.1093/gji/ggu334.
- Fukao, Y., Widiyantoro, S. & Obayashi, M., 2001. Stagnant slabs in the upper and lower mantle transition region, *Rev. Geophys.*, **39**(3), 291–323, doi: 10.1029/1999RG000068.
- Gaherty, J. B., 2001. Seismic evidence for hotspot-induced buoyant flow beneath the Reykjanes Ridge, *Science*, **293**(5535), 1645–1647, doi: 10.1126/science.106156.
- Garnero, E. J., McNamara, A. K. & Shim, S.-H., 2016. Continent-sized anomalous zones with low seismic velocity at the base of Earth's mantle, *Nature Geosci.*, **9**(7), 481–489, doi: 10.1038/NGEO2733.
- Grand, S. P., van der Hilst, R. D. & Widiyantoro, S., 1997. Global seismic tomography: A snapshot of convection in the Earth, *GSA Today*, **7**(4), 1–7.
- Hansen, S. E., Graw, J. H., Kenyon, L. M., Nyblade, A. A., Wiens, D. A., Aster, R. C., Huerta, A. D., Anandakrishnan, S. & Wilson, T., 2014. Imaging the Antarctic mantle using adaptively parameterized P-wave tomography: Evidence for heterogeneous structure beneath West Antarctica, *Earth Planet. Sci. Lett.*, **408**, 66–78, doi: 10.1016/j.epsl.2014.09.043.
- Hernlund, J. W. & Houser, C., 2008. On the statistical distribution of seismic velocities in Earth's deep mantle, *Earth Planet. Sci. Lett.*, **265**(3–4), 423–437.
- Hung, S.-H., Dahlen, F. A. & Nolet, G., 2001. Wavefront healing: a banana-doughnut perspective, *Geophys. J. Int.*, **146**, 289–312, doi: 10.1046/j.1365-246X.2001.01466.x.
- Jordan, T. H., Puster, P., Glatzmaier, G. A. & Tackley, P. J., 1993. Comparisons between seismic Earth structures and mantle flow models based on radial correlation functions, *Science*, **261**(5127), 1427–1431.
- Karato, S., 1993. Importance of anelasticity in the interpretation of seismic tomography, *Geophys. Res. Lett.*, **20**(15), 1623–1626.
- Karato, S.-I., 1998. Seismic anisotropy in the deep mantle, boundary layers and the geometry of mantle convection, *Pure Appl. Geophys.*, **151**, 565–587.
- Karato, S.-I., Jung, H., Katayama, I. & Skemer, P., 2008. Geodynamic significance of seismic anisotropy of the upper mantle: New insights from laboratory studies, *Annu. Rev. Earth Planet. Sci.*, **36**, 59–95, doi: 10.1146/annurev.earth.36.031207.124120.
- King, S. D. & Adam, C., 2014. Hotspot swells revisited, *Phys. Earth Planet. Inter.*, **235**, 66–83, doi: 10.1016/j.pepi.2014.07.006.
- Koelemeijer, P., Schubert, B. S., Davies, D. R., Deuss, A. & Ritsema, J., 2018. Constraints on the presence of post-perovskite in Earth's lowermost mantle from tomographic-geodynamic model comparisons, *Earth Planet. Sci. Lett.*, **494**, 226–238, doi: 10.1016/j.epsl.2018.04.056.
- Kohler, M. D., Hafner, K., Park, J., Irving, J. C. E., Caplan-Auerbach, J., Collins, J., Berger, J., Tréhu, A. M., Romanowicz, B. & Woodward, R. L., 2020. A plan for a long-term, automated, broadband seismic monitoring network on the global seafloor, *Seismol. Res. Lett.*, **91**(3), 1343–1355, doi: 10.1785/0220190123.
- Komatitsch, D., Barnes, C. & Tromp, J., 2000. Wave propagation near a fluid-solid interface: A spectral-element approach, *Geophysics*, **65**(2), 623–631, doi: 10.1190/1.1444758.
- Koppers, A. A. P., Becker, T. W., Jackson, M. G., Konrad, K., Müller, R. D., Romanowicz, B., Steinberger, B. & Whittaker, J. M., 2021. Mantle plumes and their role in earth processes, *Nat. Rev. Earth Env.*, **2**(6), 382–401, doi: 10.1038/s43017-021-00168-6.
- Kustowski, B., Ekström, G. & Dziewoński, A. M., 2008. Anisotropic shear-wave velocity structure of the Earth's mantle: A global model, *J. Geophys. Res.*, **113**(B6), B06306, doi: 10.1029/2007JB005169.
- Laske, G., Collins, J. A., Wolfe, C. J., Solomon, S. C., Detrick, R. S., Orcutt, J. A., Bercovici, D. & Hauri, E. H., 2009. Probing the Hawaiian hot spot with new broadband ocean bottom instruments, *Eos Trans. AGU*, **90**(41), 361–363.
- Lei, W., Ruan, Y., Bozdağ, E., Peter, D., Lefebvre, M., Komatitsch, D., Tromp, J., Hill, J., Podhorszki, N. & Pugmire, D., 2020. Global adjoint tomography—model GLAD-M25, *Geophys. J. Int.*, **223**(1), 1–21, doi: 10.1093/gji/ggaa253.
- Lekić, V. & Romanowicz, B., 2011. Inferring upper-mantle structure by full waveform tomography with the spectral element method, *Geophys. J. Int.*, **185**(2), 799–831, doi: 10.1111/j.1365-246X.2011.04969.x.
- Lekić, V., Cottaar, S., Dziewoński, A. & Romanowicz, B., 2012. Cluster analysis of global lower mantle tomography: A new class of structure and implications for chemical heterogeneity, *Earth Planet. Sci. Lett.*, **357–358**, 68–77, doi: 10.1016/j.epsl.2012.09.014.
- Li, C., van der Hilst, R. D., Engdahl, E. R. & Burdick, S., 2008. A new global model for *p* wave speed variations in Earth's mantle, *Geochim. Geophys. Geosys.*, **9**(5), Q05018, doi: 10.1029/2007GC001806.
- Li, X.-D. & Romanowicz, B., 1995. Comparison of global waveform inversions with and without considering cross-branch modal coupling, *Geophys. J. Int.*, **121**(3), 695–709, doi: 10.1111/j.1365-246X.1995.tb06432.x.
- Liu, Q. & Tromp, J., 2008. Finite-frequency sensitivity kernels for global seismic wave propagation based upon adjoint methods, *Geophys. J. Int.*, **174**, 265–286, doi: 10.1111/j.1365-246X.2008.03798.x.
- Lu, C., Grand, S. P., Lai, H. & Garnero, E. J., 2019. TX2019slab: A new *p* and *s* tomography model incorporating subducting slabs, *J. Geophys. Res.*, **124**(11), 11549–11567, doi: 10.1029/2019JB017448.
- Maggi, A., Tape, C., Chen, M., Chao, D. & Tromp, J., 2009. An automated time-window selection algorithm for seismic tomography, *Geophys. J. Int.*, **178**(1), 257–281, doi: 10.1111/j.1365-246X.2009.04099.x.
- Maguire, R., Ritsema, J., Bonnin, M., van Keken, P. E. & Goes, S., 2018. Evaluating the resolution of deep mantle plumes in teleseismic traveltimes tomography, *J. Geophys. Res.*, **123**(1), 384–400, doi: 10.1002/2017JB014730.
- Marignier, A., Ferreira, A. M. G. & Kitching, T., 2020. The probability of mantle plumes in global tomographic models, *Geochim. Geophys. Geosys.*, **21**(9), e2020GC009276, doi: 10.1029/2020GC009276.
- McNutt, M. K., 1998. Superswells, *Rev. Geophys.*, **36**(2), 211–244, doi: 10.1029/98RG00255.
- McNutt, M. K. & Fischer, K. M., 1987. The South Pacific superswell, in *Seamounts, Islands, and Atolls*, edited by B. H. Keating, P. Fryer, R. Ba-

- tiza, & G. W. Boehler, vol. 43 of **Geophysical Monograph**, pp. 25–34, doi: 10.1029/GM043, Amer. Geophys. Union.
- McNutt, M. K. & Judge, A. V., 1990. The Superswell and mantle dynamics beneath the South Pacific, *Science*, **248**(4958), 969–975, doi: 10.1126/science.1163652.
- Mégnin, C. & Romanowicz, B., 2000. The three-dimensional shear velocity structure of the mantle from the inversion of body, surface and higher-mode waveforms, *Geophys. J. Int.*, **143**(3), 709–728, doi: 10.1046/j.1365-246X.2000.00298.x.
- Montelli, R., Nolet, G., Dahlen, F. A. & Masters, G., 2006. A catalogue of deep mantle plumes: New results from finite-frequency tomography, *Geochem. Geophys. Geosys.*, **7**(11), Q11007, doi: 10.1029/2006GC001248.
- Morgan, W. J., 1971. Convection plumes in the lower mantle, *Nature*, **230**(5288), 42–43, doi: 10.1038/230042a0.
- Moulik, P., Lekić, V., Romanowicz, B., Ma, Z., Schaeffer, A., Ho, T., Beucier, E., Debayle, A., Deuss, A., Durand, S., Ekström, G., Lebedev, S., Masters, G., Priestley, K., Ritsema, J., Sigloch, K., Trampert, J. & Dziewonski, A. M., 2022. Global reference seismological data sets: multimode surface wave dispersion, *Geophys. J. Int.*, **228**(3), 1808–1849, doi: 10.1093/gji/ggab418.
- Nolet, G., Karato, S.-I. & Montelli, R., 2006. Plume fluxes from seismic tomography, *Earth Planet. Sci. Lett.*, **248**(3–4), 685–699, doi: 10.1016/j.epsl.2006.06.011.
- Nolet, G., Allen, R. & Zhao, D., 2007. Mantle plume tomography, *Chemical Geology*, **241**(3–4), 248–263, doi: 10.1016/j.chemgeo.2007.01.022.
- Nolet, G., Hello, Y., van der Lee, S., Bonnieux, S., Ruiz, M. C., Pazmino, N. A., Deschamps, A., Regnier, M. M., Font, Y., Chen, Y. J. & Simons, F. J., 2019. Imaging the Galápagos mantle plume with an unconventional application of floating seismometers, *Sci. Rep.*, **9**, 1326, doi: 10.1038/s41598-018-36835-w.
- Obayashi, M., Yoshimitsu, J., Nolet, G., Fukao, Y., Shiobara, H., Sugioka, H., Miyamachi, H. & Gao, Y., 2013. Finite frequency whole mantle p wave tomography: Improvement of subducted slab images, *GRL*, **40**(21), 5652–5657, doi: 10.1002/2013GL057401.
- Plattner, A. & Simons, F. J., 2015. High-resolution local magnetic field models for the Martian South Pole from Mars Global Surveyor data, *J. Geophys. Res.*, **120**, 1543–1566, doi: 10.1002/2015JE004869.
- Ritsema, J., Rivera, L. A., Komatitsch, D., Tromp, J. & van Heijst, H.-J., 2002. Effects of crust and mantle heterogeneity on PP/P and SS/S amplitude ratios, *Geophys. Res. Lett.*, **29**(10), 1430, doi: 10.1029/2001GL013831.
- Ritsema, J., McNamara, A. K. & Bull, A. L., 2007. Tomographic filtering of geodynamic models: Implications for model interpretation and large-scale mantle structure, *J. Geophys. Res.*, **112**, B01303, doi: 10.1029/2006JB004566.
- Ritsema, J., A. Deuss, A., van Heijst, H. J. & Woodhouse, J. H., 2011. S40RTS: a degree-40 shear-velocity model for the mantle from new Rayleigh wave dispersion, teleseismic traveltime and normal-mode splitting function measurements, *Geophys. J. Int.*, **184**, 1223–1236, doi: 10.1111/j.1365-246X.2010.04884.x.
- Ronchi, C., Iacono, R. & Paolucci, P. S., 1996. The “Cubed Sphere”: A new method for the solution of partial differential equations in spherical geometry, *J. Comput. Phys.*, **124**, 93–114, doi: 10.1006/jcph.1996.0047.
- Ruan, Y., Lei, W., Modrak, R., Örsverur, R., Bozdağ, E. & Tromp, J., 2019. Balancing unevenly distributed data in seismic tomography: a global adjoint tomography example, *Geophys. J. Int.*, **219**(2), 1225–1236, doi: 10.1093/gji/ggz356.
- Rudolph, M. L., Lekić, V. & Lithgow-Bertelloni, C., 2015. Viscosity jump in Earth’s mid-mantle, *Science*, **350**(6266), 1349–1352, doi: 10.1126/science.aad1929.
- Shen, Y., Wolfe, C. J. & Solomon, S. C., 2003. Seismological evidence for a mid-mantle discontinuity beneath Hawaii and Iceland, *Earth Planet. Sci. Lett.*, **214**(1–2), 143–151, doi: 10.1016/S0012-821X(03)00349-2.
- Shephard, G. E., Matthews, K. J., Hosseini, K. & Domeier, M., 2017. On the consistency of seismically imaged lower mantle slabs, *Sci. Rep.*, **7**(1), 10976, doi: 10.1038/s41598-017-11039-w.
- Sigloch, K. & Mihalynuk, M. G., 2013. Intra-oceanic subduction shaped the assembly of Cordilleran North America, *Nature*, **496**(7443), doi: 10.1038/nature12019.
- Simon, J. D., Simons, F. J. & Irving, J. C. E., 2021. A MERMAID miscellany: Seismoacoustic signals beyond the P wave, *Seismol. Res. Lett.*, **92**(6), 3657–3667, doi: 10.1785/0220210052.
- Simon, J. D., Simons, F. J. & Irving, J. C. E., 2022. Recording earthquakes for tomographic imaging of the mantle beneath the South Pacific by autonomous MERMAID floats, *Geophys. J. Int.*, **228**, 147–170, doi: 10.1093/gji/ggab271.
- Slack, P. D., Fox, C. G. & Dziak, R. P., 1999. P wave detection thresholds, P_n velocity estimates, and T wave location uncertainty from oceanic hydrophones, *J. Geophys. Res.*, **104**(B6), 13061–13072, doi: 10.1029/1999JB900112.
- Sleep, N. H., 1990. Hotspots and mantle plumes: Some phenomenology, *J. Geophys. Res.*, **95**(B5), 6715–6736, doi: 10.1029/JB095iB05p06715.
- Steinberger, B., 2000. Plumes in a convecting mantle: Models and observations for individual hotspots, *J. Geophys. Res.*, **105**(B5), 11127–11152, doi: 10.1029/1999JB900398.
- Steinberger, B., Sutherland, R. & O’Connell, R. J., 2004. Prediction of Emperor-hawaii seamount locations from a revised model of global plate motion and mantle flow, *Nature*, **430**, 167–173, doi: 10.1038/nature02660.
- Sukhovich, A., Irissou, J.-O., Perrot, J. & Nolet, G., 2014. Automatic recognition of T and teleseismic P waves by statistical analysis of their spectra: An application to continuous records of moored hydrophones, *J. Geophys. Res.*, **119**(8), 6469–6485, doi: 10.1002/2013JB010936.
- Sukhovich, A., Bonnieux, S., Hello, Y., Irissou, J.-O., Simons, F. J. & Nolet, G., 2015. Seismic monitoring in the oceans by autonomous floats, *Nat. Commun.*, **6**, 8027, doi: 10.1038/ncomms9027.
- Tshekmistrenko, M., Sigloch, K., Hosseini, K. & Barruol, G., 2021. A tree of Indo-African mantle plumes imaged by seismic tomography, *Nature Geosci.*, **14**(8), 612–619, doi: 10.1038/s41561-021-00762-9.
- van der Hilst, R. D., Engdahl, E. R. & Spakman, W., 1993. Tomographic inversion of P -data and pP -data for aspherical mantle structure below the northwest Pacific region, *Geophys. J. Int.*, **115**(1), 264–302.
- Wamba, M. D., Montagner, J.-P., Romanowicz, B. & Barruol, G., 2021. Multi-mode waveform tomography of the Indian Ocean upper and mid-mantle around the Réunion hotspot, *J. Geophys. Res.*, **126**, e2020JB021490, doi: 10.1029/2020JB021490.
- Wamba, M. D., Montagner, J.-P. & Romanowicz, B., 2023. Imaging deep-mantle plumbing beneath La Réunion and Comores hot spots: Vertical plume conduits and horizontal ponding zones, *Sci. Adv.*, **9**(4), eade3723, doi: 10.1126/sciadv.ade3723.
- Wang, Z. & Dahlen, F. A., 1995. Spherical-spline parameterization of three-dimensional Earth models, *Geophys. Res. Lett.*, **22**(22), 3099–3102, doi: 10.1029/95GL03080.
- Webb, S. C. & Crawford, W. C., 2010. Shallow-water broadband OBS seismology, *B. Seismol. Soc. Am.*, **100**(4), 1770–1778, doi: 10.1785/0120090203.
- Weis, D., Harpp, K. S., Harrison, L. N., Boyet, M., Chauvel, C., Farnetani, C. G., Finlayson, V. A., Lee, K. K. M., Parai, R., Shahar, A. & Williamson, N. M. B., 2023. Earth’s mantle composition revealed by mantle plumes, *Nat. Rev. Earth Env.*, **4**, 604–625, doi: 10.1038/s43017-023-00467-0.
- Williams, C. D., Mukhopadhyay, S., Rudolph, M. L. & Romanowicz, B., 2019. Primitive helium is sourced from seismically slow regions in the lowermost mantle, *Geochem. Geophys. Geosys.*, **20**(8), 4130–4145, doi: 10.1029/2019GC008437.

- Wolfe, C. J., Solomon, S. C., Laske, G., Collins, J. A., Detrick, R. S., Orcutt, J. A., Bercovici, D. & Hauri, E. H., 2009. Mantle shear-wave velocity structure beneath the Hawaiian hot spot, *Science*, **326**(5958), 1388–1390, doi: 10.1126/science.1180165.
- Yu, C., Day, E. A., de Hoop, M. V., Campillo, M., Goes, S., Blythe, R. A. & van der Hilst, R. D., 2018. Compositional heterogeneity near the base of the mantle transition zone beneath Hawaii, *Nat. Commun.*, **9**, 1266, doi: 10.1038/s41467-018-03654-6.
- Zhang, Z., Irving, J. C. E., Simons, F. J. & Alkhalifah, T., 2023. Seismic evidence for a 100 km mantle discontinuity under the Pacific, *Nat. Commun.*, **14**, 1714, doi: 10.1038/s41467-023-37067-x.
- Zhao, D., 2004. Global tomographic images of mantle plumes and subducting slabs: insight into deep Earth dynamics, *Phys. Earth Planet. Inter.*, **146**(1–2), 3–34.
- Zhu, H., Bozdağ, E., Peter, D. & Tromp, J., 2012. Structure of the European upper mantle revealed by adjoint tomography, *Nature Geosci.*, **5**(7), 493–498, doi: 10.1038/ngeo1501.